## PAPER

Check for updates

# Rational synthesis of a hierarchical Mo₂C/C nanosheet composite with enhanced lithium storage properties†

Xin Yue, Minglei Cao, [ID] * Limeng Wu, Wei Chen, Xingxing Li, Yanan Ma [ID] and Chuankun Zhang*

Transition metal carbides have been studied extensively as anode materials for lithium-ion batteries (LIBs), but they suffer from sluggish lithium reaction kinetics and large volume expansion. Herein, a hierarchical Mo₂C/C nanosheet composite has been synthesized through a rational pyrolysis strategy, and evaluated as an anode material with enhanced lithium storage properties for LIBs. In the hierarchical Mo₂C/C nanosheet composite, large numbers of Mo₂C nanosheets with a thickness of 40–100 nm are uniformly anchored onto/into carbon nanosheet matrices. This unique hierarchical architecture can provide favorable ion and electron transport pathways and alleviate the volume change of Mo₂C during cycling. As a consequence, the hierarchical Mo₂C/C nanosheet composite exhibits high-performance lithium storage with a reversible capacity of up to 868.6 mA h g⁻¹ after 300 cycles at a current density of 0.2 A g⁻¹, as well as a high rate capacity of 541.8 mA h g⁻¹ even at 5.0 A g⁻¹. More importantly, this hierarchical composite demonstrates impressive cyclability with a capacity retention efficiency of 122.1% over 5000 successive cycles at 5.0 A g⁻¹, which surpasses the cycling properties of most other Mo₂C-based materials reported to date.

## Introduction

Lithium-ion batteries (LIBs) have become one of the most important power sources, with applications from intelligent electronic devices and electric vehicles to grid-scale energy storage systems.[1–3] However, graphite, a most common commercial anode material for LIBs, is far from satisfactory due to its low theoretical capacity of 372 mA h g⁻¹, which is unable to meet the ever-increasing energy demand. Furthermore, graphite exhibits a short cycling life and severe safety issues arising from the formation of unstable SEI layers and lithium dendrites during cycling.[4–6] Over the last decade, transition metal oxides and sulfides have been considered as promising alternative anode materials for LIBs on account of their large theoretical capacity, high electrochemical reactivity and abundant natural resources.[7–10] Nevertheless, they suffer from inferior rate capability and rapid capacity fading because of their large volume change and poor electronic conductivity. Hence, it is highly desirable to develop advanced anode materials simultaneously with high capacity, superior rate capability and long-term cyclability for high-performance LIBs.

In recent years, transition metal carbides have been studied extensively as anode materials for LIBs.[11–13] Specifically,

molybdenum carbide (Mo₂C) have received much attention in light of its large theoretical capacity, favorable electric conductivity, as well as good chemical and mechanical stability.[14–16] However, the sluggish lithium-ion transport kinetics and large volume expansion inevitably lead to poor rate performance and rapid capacity fading for this material. To tackle these challenges, one of the most effective methods is to design and construct the composites of Mo₂C and carbon, in which the volume expansion of Mo₂C can be relieved, as well as the charge transport properties can be significantly improved. For instance, Zhu *et al.*[17] reported Mo₂C/N-doped carbon mesoporous heteronanowires as suitable anode materials for LIBs, manifesting a reversible capacity of 941.1 mA h g⁻¹ over 50 cycles at 0.1 A g⁻¹. Lu and co-workers[18] synthesized porous N,P co-doped Mo₂C/C nanosheets through calcining a chitosan–Mo composite hydrogel. The carbon nanosheet matrix can facilitate fast ion and electron transports and mitigate the volume expansion of Mo₂C during cycling. Mo₂C@C core–shell nanocrystals on 3D graphene hybrid aerogel was successfully synthesized and studied as LIBs anode material,[19] which retained a charge capacity of 1089.8 mA h g⁻¹ over 100 cycles at 0.1 A g⁻¹ and achieved a high rate capacity of 623.5 mA h g⁻¹ at 5 A g⁻¹. These previous works have verified the potential of employing Mo₂C/C composites as anode materials for high-performance LIBs, whereas their cycling performance should be further improved. Hence, more researches should be devoted to enhance the cycling performance of Mo₂C/C composites by

*School of Sciences, Hubei University of Automotive Technology, Shiyan 442002, P. R. China. E-mail: cml07114052@163.com; zhangchk_lx@huat.edu.cn*

† Electronic supplementary information (ESI) available. See DOI: 10.1039/d1ra03822b

optimizing the morphology and architecture of $Mo_2C/C$ composites, thus achieving robust lithium reaction kinetics and simultaneously alleviating the volume expansion of $Mo_2C$. Meanwhile, it is of significant importance to develop more effective and economical methods to synthesize the $Mo_2C/C$ composites.

In this report, $Mo_2C/C$ nanosheet composites were fabricated with a rational pyrolysis method using sodium chloride (NaCl) as templates. The cubic NaCl crystals can easily self-assemble and create a 2D spatial confinement to obtain the $Mo_2C/C$ nanosheet composites. By optimizing the carbon content of the composites, the product (denoted as $Mo_2C/C$-2) presents a unique hierarchical architecture, in which $Mo_2C$ nanosheets uniformly grow onto/into carbon nanosheets matrices. This architecture endows the $Mo_2C/C$-2 with several structural and kinetic advantages for electrochemical lithium storage, such as good structural integrality, slight volume expansion, and fast ion and electron transport properties. Hence, the $Mo_2C/C$-2 demonstrates an initial discharge capacity of up to 1057.3 mA h $g^{-1}$ at 0.2 A $g^{-1}$, and retains a reversible capacity of 532.1 mA h $g^{-1}$ (122.1% capacity retention efficiency) after 5000 consecutive cycles at 5.0 A $g^{-1}$. It is worth noting that the outstanding cycle life of the hierarchical $Mo_2C/C$ nanosheet composite surpasses the cycling properties of most other $Mo_2C$-based materials reported to date.

## Experimental

### Preparation of hierarchical $Mo_2C/C$ nanosheet composite

In a typical synthesis, 3 mmol of $Na_2MoO_4 \cdot 2H_2O$, 1 mmol of $C_6H_{12}O_6$, and 25 mmol of NaCl were dissolved in 60 mL deionized water through magnetic stirring. Subsequently, the above mixed solution was placed in an oven and heated rapidly to 80 °C until fully evaporation of the water. The resultant brown precipitate was grinded into very fine powders and then sintered at 800 °C for 2 h with a ramp rate of 5 °C $min^{-1}$ in Ar atmosphere. Finally, the final product ($Mo_2C/C$-2) was collected by centrifugation and rinsed in distilled water and ethanol, followed by drying at 80 °C under vacuum. For comparison, the $Mo_2C/C$ nanosheet composites synthesized through the identical procedures but using 0.5 and 2 mmol of $C_6H_{12}O_6$ were marked as $Mo_2C/C$-1 and $Mo_2C/C$-3, respectively. Additionally, pure carbon (denoted as p-C) and $Mo_2C/C$ composite ($Mo_2C/C$-4) were prepared through the identical procedures without use of $Na_2MoO_4 \cdot 2H_2O$ and NaCl, respectively.

### Material characterization

The phase composition and crystallinity of the as-prepared $Mo_2C/C$ composites were characterized by X-ray diffraction (XRD) measurement using an X'Pert 3 X-ray diffractometer (Cu Kα radiation, $2\theta$ range of 20–80°). A Thermo scientific FT-Raman spectrometer (Nd-line laser source with 532 nm wavelength) was used for collecting the Raman spectra of the samples. The carbon contents in the as-prepared $Mo_2C/C$ composites were measured by thermogravimetric analysis (TGA, Q600) in air. X-ray photoelectron spectroscopy (XPS,

Thermo Scientific K-Alpha) measurements were conducted to investigate the elemental composition and surface chemical state of the samples. The morphological and structural features of the obtained products were studied using Field emission scanning electron microscopy (FSEM, FEI Nova NanoSEM 450) and transmission electron microscopy (TEM, FEI Titan $G^2$ 60–300), equipped with energy dispersive spectroscope (EDS).

### Electrochemical measurements

The working electrode was made by pasting the slurry consisting of 80 wt% $Mo_2C/C$ nanosheet composites, 10 wt% acetylene black, and 10 wt% polytetrafluoroethylene onto copper foil using N-methyl-2-pyrrolidinone as a solvent. The coated copper foils were dried overnight in a vacuum oven at 80 °C, and then cut into 14 mm circular disks. The average mass loading of the active materials ($Mo_2C/C$ nanosheet composites) was around 1.2 mg $cm^{-2}$. The CR-2032 coin cells were fabricated in an Ar-filled dry glove box using metallic lithium foils as the counter/reference electrodes and Celgard 2400 polypropylene membranes as the separators. The electrolyte consists of 1 M $LiPF_6$ in a solution of EC and DEC in a 1 : 1 volume ratio. Galvanostatic charge/discharge tests were conducted in the potential window of 0.01–3.0 V (vs. $Li/Li^+$) on a LAND-CT2001C tester. Cyclic voltammetry (CV) curves were obtained using an electrochemical workstation (CHI660E) at different scanning rates within the potential range from 0.01 to 3.0 V. Electrochemical impedance spectroscopy (EIS) measurements were performed on the CHI660E workstation in the frequency range between 100 kHz and 10 mHz with a sine wave of 5 mV.

## Results and discussion

### Material preparation and characterization

As schematically illustrated in Fig. 1, the preparation route of hierarchical $Mo_2C/C$ nanosheet composite mainly involves
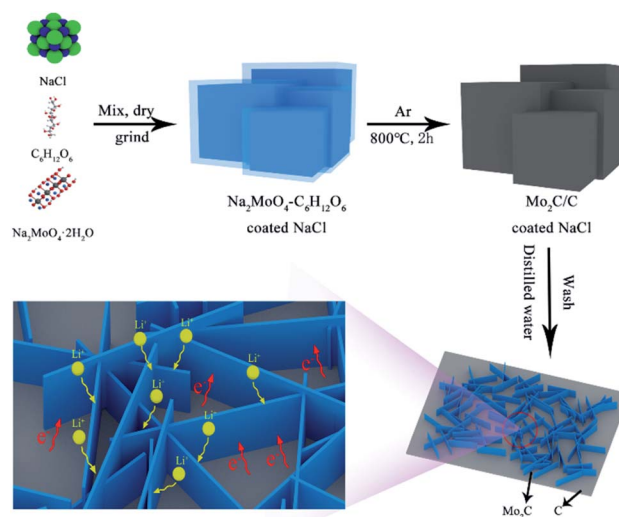


**Fig. 1** Schematic illustration of fabrication of hierarchical $Mo_2C/C$ nanosheet composite.

three main steps. The first step is formation of the intermediate complex of $Na_2MoO_4$–$C_6H_{12}O_6$ coated NaCl by dissolving these chemicals in deionized water and then completely evaporating the water. Subsequently, the intermediate product is annealed under Ar atmosphere at 800 °C to obtain the composite of $Mo_2C$/C coated NaCl. Finally, the NaCl templates are removed by wash with water, thus resulting in the formation of hierarchical $Mo_2C$/C nanosheet composite. Owing to its kinetic and structural merits, the hierarchical $Mo_2C$/C nanosheet composite could exhibit high $Li^+$ accessibility, favorable electron transport pathways and good structural integrity.

Fig. 2a displays the XRD patterns of the various $Mo_2C$/C composites. Sharp diffraction peaks can be seen for all these three samples, which indicates good crystallinity of the $Mo_2C$/C composites. The diffraction peaks at 2-theta of 34.4, 37.9, 39.4, 52.1, 61.6, 69.6, 72.5, 74.7 and 75.6° can be assigned to the (100), (002), (101), (102), (110), (103), (200), (112) and (201) crystal planes of hexagonal $Mo_2C$ (JCPDS no. 35-0787), respectively.[20,21] Obviously, the peak intensity becomes weaker with increasing the carbon content in the composites. In addition, no diffraction peak pertaining to carbon species is detected in the XRD patterns, thus implying the carbon is in amorphous state. To get a deeper understanding of the carbon structure in the $Mo_2C$/C composites, Raman characterization were performed. As seen in Fig. 2b, all the products reveal two obvious Raman peaks and the peak intensity grows stronger with the increase of carbon content. The characteristic peaks located at about 1345 and 1592 $cm^{-1}$ can be attributed to the D and G bands of the amorphous carbon, respectively. Specifically, the D band associates with the disordered planes and defects in graphitic structure, while the G band originates from the $sp^2$-hybridized carbon atoms.[22,23] Herein, the intensity ratios ($I_D/I_G$) of D band to G band are 1.32 for $Mo_2C$/C-1, 1.06 for $Mo_2C$/C-2, and 1.04 for $Mo_2C$/C-3, which manifest the presence of abundant carbon component with rich defects.

The elemental composition and surface chemical state of $Mo_2C$/C-2 were analyzed by XPS. Fig. S1† shows the XPS survey

spectrum, which confirms the presence of Mo, C and O elements within this material. As depicted in Fig. 2c, the high-resolution Mo 3d spectrum can be fitted into three doublets. The peaks with binding energies at 228.6 and 231.7 eV are assigned to $Mo^{2+}$ from $Mo_2C$, and the other two pairs of peaks are ascribed to $Mo^{4+}$ (229.3/233.1 eV) and $Mo^{6+}$ (232.6/235.8 eV) in molybdenum oxidized phases associated with the surface oxidation of $Mo_2C$.[20,24] The high-resolution spectrum of C 1s (Fig. 2d) contains three peaks with binding energies at 283.6, 285.3, and 288.0 eV, which can be attributed to C–Mo, C–C, and O–C=O, respectively.[20,25] The carbon contents in the various $Mo_2C$/C composites are determined based on TGA. As shown in Fig. S2,† the TGA curves for all the three samples display a weight loss in the temperature range from 370 to 500 °C, which can be attributed to the combustion of the carbon component. Above 600 °C, no weight change is observed in all the TGA curves, indicating the $Mo_2C$ is fully converted into $MoO_3$ in air.[16,24] Based on the thermal properties of the $Mo_2C$/C composites, the carbon contents can be calculated using formula (S1) (see in ESI†). Hence, the carbon contents in $Mo_2C$/C-1, $Mo_2C$/C-2, and $Mo_2C$/C-3 are 3.8%, 14.0%, and 22.2%, respectively.

Fig. 3 presents the SEM images of the various $Mo_2C$/C composites. Numerous small $Mo_2C$ nanosheets and large carbon nanosheet matrices are clearly observed, forming $Mo_2C$/C nanosheet composites. The thickness of the $Mo_2C$ nanosheets is within the range of 40–100 nm. As seen in Fig. 3a and d, the $Mo_2C$ nanosheets agglomerate into a sphere-like structure for $Mo_2C$/C-1, this could be attributed to the low carbon content in this sample. Owing to the suitable amount of carbon in $Mo_2C$/C-2 (Fig. 3b and e), the $Mo_2C$ nanosheets uniformly grow onto/into the carbon nanosheet matrices. This unique architecture could significantly enhance electrochemical lithium storage properties in consideration of the favourable ion and electron transport pathways and good structural integrity. With further increasing the carbon content, the thickness of the carbon nanosheet matrices becomes thicker and the $Mo_2C$ nanosheets agglomerate into sphere-like structure on the carbon matrices again (Fig. 3c and f). According to the SEM analysis, it can be concluded that the carbon content plays a vital role in
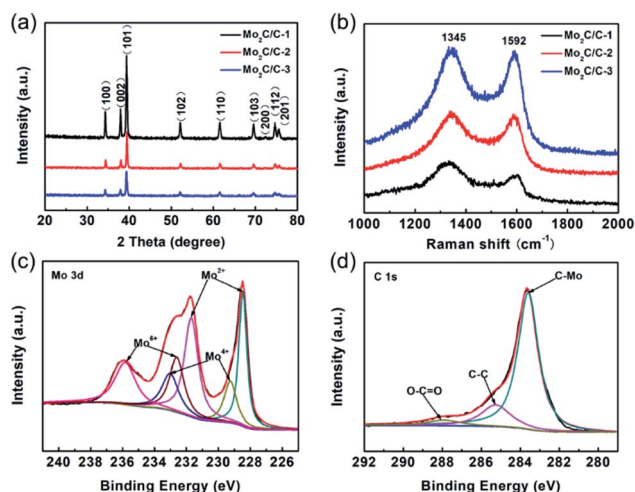


**Fig. 2** (a) XRD patterns and (b) Raman spectra of various $Mo_2C$/C composites; high-resolution XPS spectra of (c) Mo 3d and (d) C 1s.
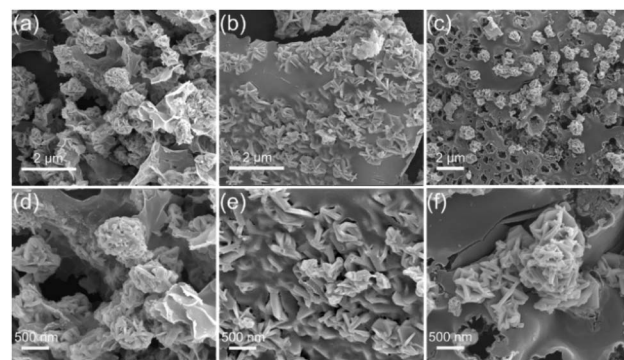


**Fig. 3** SEM images of (a and d) $Mo_2C$/C-1, (b and e) $Mo_2C$/C-2, and (c and f) $Mo_2C$/C-3 with different magnification.
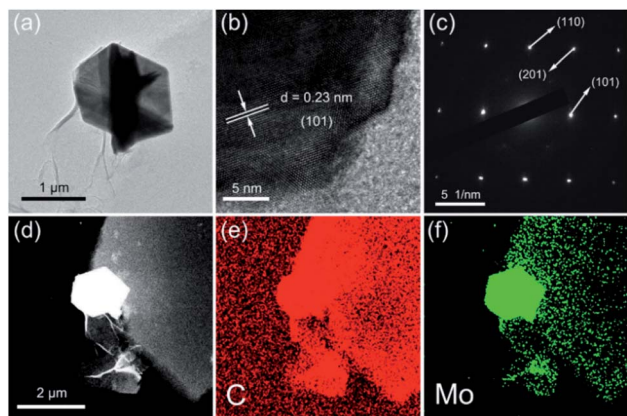
**Fig. 4** (a) TEM and (b) HR-TEM images of Mo$_2$C/C-2; (c) SAED pattern of the Mo$_2$C/C-2; EDS mapping images of (d) the Mo$_2$C/C-2 and the elements of (e) C, (f) Mo, respectively.

controlling the morphology of Mo$_2$C/C composites, thus largely affects the lithium storage properties.

Further insights into the morphology and microstructure of Mo$_2$C/C-2 were elucidated by TEM. As displayed in Fig. 4a, the Mo$_2$C nanosheets are interconnected to anchored on carbon nanosheet matrices. The high resolution TEM (HR-TEM) image of the edge of Mo$_2$C nanosheet is shown in Fig. 4b, in which



**Fig. 5** (a) Initial three CV curves of Mo$_2$C/C-2 at the scan rate of 0.1 mV s$^{-1}$; (b) initial galvanostatic profiles of Mo$_2$C/C-1, Mo$_2$C/C-2 and Mo$_2$C/C-3 at the current density of 0.2 A g$^{-1}$; (c) cycling performance comparison of Mo$_2$C/C-1, Mo$_2$C/C-2 and Mo$_2$C/C-3 at the current density of 0.2 A g$^{-1}$; (d) rate performance of Mo$_2$C/C-1, Mo$_2$C/C-2 and Mo$_2$C/C-3 at various current densities from 0.1 to 5.0 A g$^{-1}$; (e) long-term cycling performance of Mo$_2$C/C-2 at the high current density of 5.0 A g$^{-1}$.

well-crystallized structure of the Mo$_2$C nanosheet can be clearly observed. The lattice fringe with an interplanar spacing of 0.23 nm is in agreement well with the (101) plane of Mo$_2$C.[24,25] The carbon matrices show no lattice fringe, being a further proof of their amorphous state. As seen in Fig. 4c, the SAED pattern reveals single crystalline nature of the Mo$_2$C nanosheets, and the lattice spaces are well matched to the (101), (110) and (201) planes of the Mo$_2$C phase.[18,21] Additionally, the EDS mapping images are displayed in Fig. 4d–f, which demonstrate the Mo$_2$C nanosheets are fixed on carbon nanosheets matrice and the hierarchical nanosheet composite consists of the elements of Mo and C.

### Electrochemical and kinetic characteristics

We then evaluated the lithium storage performances of the Mo$_2$C/C nanosheet composites in half-cells using metallic lithium foils as counter/reference electrodes. Fig. 5a depicts the initial three CV curves of Mo$_2$C/C-2 at 0.1 mV s$^{-1}$. In the first CV curve, a prominent cathodic peak ($\sim$1.07 V) is observed, which is related to the formation of SEI and conversion reaction of Mo$_2$C to Mo. In addition, the cathodic peak at about 0.62 V can be ascribed to the lithiation of carbon matrices.[25,26] The CV curves almost completely overlap and exhibit one pair of redox peaks occurring at $\sim$1.21/1.42 V in the subsequent cycles, indicating that the conversion reaction of Mo$_2$C with Li$^+$ is highly reversible and stable.[18,27] Fig. 5b presents the first galvanostatic charge/discharge curves of the samples. The initial discharge capacities of Mo$_2$C/C-1, Mo$_2$C/C-2 and Mo$_2$C/C-3 are 1203.1, 1057.3 and 931.8 mA h g$^{-1}$ at 0.2 A g$^{-1}$, respectively, with coulombic efficiencies of 55.9%, 61.6% and 56.2%. Obviously, the electrochemical properties of the Mo$_2$C/C nanosheet composites are greatly affected by their carbon content. The discharge capacities of the samples become lager with reducing carbon content. Nevertheless, an optimal carbon content is necessary to get a high coulombic efficiency. Fig. S3† shows the charge/discharge curves of the various Mo$_2$C/C nanosheet composites at different cycles. The Mo$_2$C/C-2 exhibits a smallest voltage separation between the charge and discharge curves as compared to Mo$_2$C/C-1 and Mo$_2$C/C-3, revealing lowest electrochemical polarization, which could be ascribed to the fast ion and electron transport properties of the hierarchical nanosheet architecture.

Fig. 5c compares the cycling performance of the composites with various carbon contents. The Mo$_2$C/C-2 displays much higher capacity from the 60th cycle onwards as compared to Mo$_2$C/C-1 and Mo$_2$C/C-3. Interestingly, the capacities of Mo$_2$C/C-2 and Mo$_2$C/C-3 becomes larger during the cycling process. This may result from an electrochemical activation process of Mo$_2$C with the electrolyte gradually permeating into the nanosheet composites because of the existence of carbon with relative high content in those two composites. After 300 cycles, the reversible capacity of Mo$_2$C/C-2 reaches to 868.6 mA h g$^{-1}$ with 133.4% capacity retention efficiency. Nevertheless, the similarly cycled Mo$_2$C/C-1 and Mo$_2$C/C-3 deliver reversible capacities of 566.7 and 586.2 mA h g$^{-1}$, which are 84.1% and 112.0% of their initial values, respectively. The morphological and structural
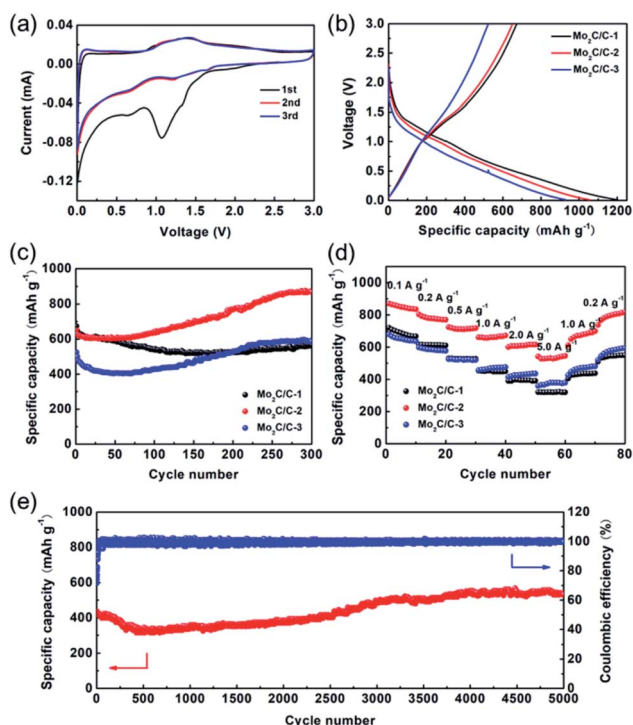
evolutions of the various $Mo_2C/C$ nanosheet composites after cycling test were investigated in details through SEM analysis (Fig. S4†). The results demonstrate that the $Mo_2C/C$-2 exhibits best structural integrity and smallest volume change after cycling, which supports the excellent cycling stability of this material. Additionally, the electrochemical performances of p-C and $Mo_2C/C$-4 were investigated. As seen in Fig. S5a and c,† the p-C delivers low initial discharge (245.8 mA h g$^{-1}$) and charge (123.3 mA h g$^{-1}$) capacities and it maintains a reversible capacity of 121.2 mA h g$^{-1}$ over 200 cycles. Though a relative high initial discharge capacity (1013.8 mA h g$^{-1}$) is achieved, the charge capacity is only 406.9 mA h g$^{-1}$ for $Mo_2C/C$-4 (Fig. S5b and d†). After 200 cycles, the reversible capacity of $Mo_2C/C$-4 is 449.7 mA h g$^{-1}$, which is much lower than that of the similar cycled $Mo_2C/C$-2 (767.3 mA h g$^{-1}$).

The rate performance of the various $Mo_2C/C$ nanosheet composites (over 300 cycles at 0.2 A g$^{-1}$) was explored at different current densities ranging up from 0.1 to 5.0 A g$^{-1}$. As displayed in Fig. 5d, the $Mo_2C/C$-2 reveals much higher capacity than $Mo_2C/C$-1 and $Mo_2C/C$-3 at every current density. The reversible capacities of $Mo_2C/C$-2 are 871.3, 803.9, 725.1, 661.3, 600.8 and 541.8 mA h g$^{-1}$ at 0.1, 0.2, 0.5, 1.0, 2.0 and 5.0 A g$^{-1}$, respectively. Impressively, the $Mo_2C/C$-2 is still able to provide capacities of 699.9 and 818.2 mA h g$^{-1}$ when coming back to 1.0 and 0.2 A g$^{-1}$, respectively, signifying favorable rate reversibility. In order to exploit its long-term cycling stability, the $Mo_2C/C$-2 was cycled at the high current density of 5.0 A g$^{-1}$ (Fig. 5e). Though the capacity of $Mo_2C/C$-2 undergoes a declining process in the first 500 cycles, it increases to 532.1 mA h g$^{-1}$ over 5000 cycles, with a capacity retention efficiency of 122.1%. We note this outstanding cycle life of $Mo_2C/C$-2 is superior to those of most other $Mo_2C$-based materials reported to date (Table S1†).[15,17–19,25,27–29] Meanwhile, the $Mo_2C/C$-2 exhibits high coulombic efficiencies of around 100% from the 30th cycle onwards, revealing that the lithium storage of this hierarchical nanosheet composite is highly reversible.

To deeply explore the lithium storage behavior, the lithium reaction kinetics of the hierarchical nanosheet composite was performed with the CV measurements at various sweep rates between 0.1 and 5.0 mV s$^{-1}$. As depicted in Fig. 6a, the $Mo_2C/C$-2 presents highly similar CV profiles and slight voltage delay with increasing the sweep rate, manifesting a fast pseudocapacitive lithium storage process that is independent of sweep rate. The total charge storage can be categorized into surface-controlled (capacitive) effect and diffusion-controlled (battery) process, and therefore the current response ($i$) and sweep rate ($v$) can be described as following relationship:[30,31]

$$i = av^b \tag{1}$$

$$\log(i) = b\log(v) + \log(a) \tag{2}$$

in which $a/b$ are empirical parameters. The lithium storage behavior depends on the $b$-value, which derives from slope of the $\log(i)$ vs. $\log(v)$ plot. When the $b$-value is 0.5, a typical diffusion-controlled (battery) process can be identified. Whereas, the $b$-value of 1.0 suggests that the electrochemical
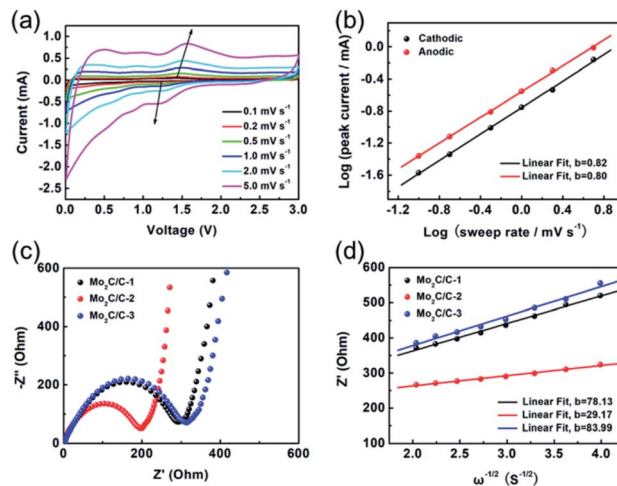


**Fig. 6** (a) CV curves of $Mo_2C/C$-2 at sweep rates from 0.1 to 5.0 mV s$^{-1}$; (b) relationship between the peak currents and scan rates in their logarithmic format for $Mo_2C/C$-2; (c) Nyquist plots of $Mo_2C/C$-1, $Mo_2C/C$-2 and $Mo_2C/C$-3 at fresh coin cells; (d) corresponding linear fits of the $Z'$ versus $\omega^{-1/2}$ in the low-frequency region.

reaction is determined with an ideal surface-controlled (capacitive) behavior. According to Fig. 6b, the $b$-values of cathodic peaks and anodic peaks for $Mo_2C/C$-2 are 0.82 and 0.8 respectively, which further demonstrates a typical pseudocapacitive behavior with fast lithium storage kinetics.

In addition, EIS analysis was carried out to understand the charge transport properties of the $Mo_2C/C$ nanosheet composites. Fig. 6c depicts the Nyquist plots of $Mo_2C/C$-1, $Mo_2C/C$-2 and $Mo_2C/C$-3 at fresh coin cells. A depressed semicircle can be observed at high frequencies, which is related to the resistances of the charge transfer ($R_{ct}$) and SEI films ($R_f$). Meanwhile, the inclined line in low frequencies region is ascribed to Warburg-type resistance ($W_1$) corresponding to ion diffusion within electrode.[32,33] The equivalent circuit model shown in Fig. S6† can be used to fit the datum of the impedance spectra. The $Mo_2C/C$-2 electrode delivers a smallest $R_{ct}$ value of 202.1 Ω (295.7 Ω for $Mo_2C/C$-1 electrode, 317.9 Ω for $Mo_2C/C$-3 electrode), indicating fastest interface charge transfer for this electrode.[8,34] This can be explained by the favorable electron transport between $Mo_2C$ and carbon matrices in the hierarchical nanosheet architecture of $Mo_2C/C$-2. Fig. S7† displays the Nyquist plots of the various $Mo_2C/C$ nanosheet composites during cycling test. Both the $Mo_2C/C$-2 and $Mo_2C/C$-3 exhibit much larger decline in the resistances of $R_{ct}$ and $R_f$ as compared to $Mo_2C/C$-1, indicating the existence of an obvious activation process during cycling, which supports the phenomenon of capacity increase for the $Mo_2C/C$-2 and $Mo_2C/C$-3. Additionally, the diffusion coefficient of Li$^+$ ($D_{Li^+}$) in the various $Mo_2C/C$ nanosheet composites can be calculated from Warburg region using the formula (3):[35,36]

$$D_{Li^+} = R^2T^2/2A^2n^4F^4C^2\sigma^2 \tag{3}$$

$$Z' = R + \sigma\omega^{-1/2} \tag{4}$$

where $R$, $T$, $F$, $A$, $n$ and $C$ are the universal gas constant, the absolute temperature, the Faraday constant, the surface area of working electrode, the electrons number per molecule during redox reaction, the molar concentration of Li$^+$, respectively. Besides, $\sigma$ is the Warburg factor, which is associated with $Z'$ (formula (4)).[37,38] As seen in Fig. 6d, the $\sigma$ was obtained from the slope of the fitting line of $Z'$ and $\omega^{-1/2}$ in the Warburg region. The $D_{Li^+}$ value of Mo$_2$C/C-2 is $2.59 \times 10^{-10}$ cm$^2$ s$^{-1}$, which is much higher than those of Mo$_2$C/C-1 ($3.61 \times 10^{-11}$ cm$^2$ s$^{-1}$) and Mo$_2$C/C-3 ($3.12 \times 10^{-11}$ cm$^2$ s$^{-1}$). Consequently, the EIS results confirm the fast ion and electron transport properties of Mo$_2$C/C-2, which could be ascribed to the favorable charge transport pathways of the unique hierarchical nanosheet architecture.

## Conclusions

In conclusion, we report a rational pyrolysis approach to synthesize Mo$_2$C/C nanosheet composites using cubic NaCl crystals as the templates. The morphology of the Mo$_2$C/C nanosheet composites can be controlled with the carbon content and a unique hierarchical architecture is obtained. The Mo$_2$C nanosheets exhibit a thickness of 40–100 nm and uniformly grow onto/into the carbon nanosheet matrices. This unique architecture can facilitate fast ion and electron transports between Mo$_2$C and carbon matrices and maintain good structural stability, thus resulting in high-performance lithium storage. As a consequence, the hierarchical Mo$_2$C/C nanosheet composite exhibits a reversible capacity of 868.6 mA h g$^{-1}$ at 0.2 A g$^{-1}$ over 300 cycles, and a high rate capacity of 541.8 mA h g$^{-1}$ still can be achieved even at 5.0 A g$^{-1}$. Impressively, the hierarchical Mo$_2$C/C nanosheet composite demonstrates excellent cyclability with a capacity retention efficiency of 122.1% after 5000 successive cycles at 5.0 A g$^{-1}$. The high capacity and outstanding cycle life demonstrate the good application prospect in high-performance LIBs for the hierarchical Mo$_2$C/C nanosheet composite.

## Author contributions

Xin Yue: data curation, writing – original draft; Minglei Cao: conceptualization, writing – review & editing, funding acquisition; Limeng Wu: data curation; Wei Chen: data curation; Xingxing Li: writing – review & editing; Yanan Ma: funding acquisition; Chuankun Zhang: writing – review & editing, supervision.

## Conflicts of interest

There are no conflicts to declare.

## Acknowledgements

## Notes and references

1 J. M. Tarascon and M. Armand, *Nature*, 2001, **414**, 359.
2 J. W. Choi and D. Aurbach, *Nat. Rev. Mater.*, 2016, **1**, 1.
3 P. Yang and J. M. Tarascon, *Nat. Mater.*, 2012, **11**, 560.
4 A. Mukhopadhyay, A. Tokranov, X. Xiao and B. W. Sheldon, *Electrochim. Acta*, 2012, **66**, 28.
5 Y. F. Ma, H. C. Chang, M. Zhang and Y. S. Chen, *Adv. Mater.*, 2015, **27**, 5296.
6 P. Roy and S. K. Srivastava, *J. Mater. Chem. A*, 2015, **3**, 2454.
7 Y. Zhao, X. Li, B. Yan, D. Xiong, D. Li, S. Lawes and X. Sun, *Adv. Energy Mater.*, 2016, **6**, 1502175.
8 M. Cao, L. Tao, X. Lv, Y. Bu, M. Li, H. Yin, M. Zhu, Z. Zhong, Y. Shen and M. Wang, *J. Power Sources*, 2018, **396**, 327.
9 S. Fang, D. Bresser and S. Passerini, *Adv. Energy Mater.*, 2020, **10**, 1902485.
10 Q. Li, H. Li, Q. Xia, Z. Hu, Y. Zhu, S. Yan, C. Ge, Q. Zhang, X. Wang, X. Shang, S. Fan, Y. Long, L. Gu, G. X. Miao, G. Yu and J. S. Moodera, *Nat. Mater.*, 2021, **20**, 76.
11 X. Chen, Z. Kong, N. Li, X. Zhao and C. Sun, *Phys. Chem. Chem. Phys.*, 2016, **18**, 32937.
12 M. Q. Zhao, M. Torelli, C. E. Ren, M. Ghidiu, Z. Ling, B. Anasori, M. W. Barsoum and Y. Gogotsi, *Nano Energy*, 2016, **30**, 603.
13 Y. Zhong, X. Xia, F. Shi, J. Zhan, J. Tu and H. J. Fan, *Adv. Sci.*, 2016, **3**, 1500286.
14 Q. C. Zhu, S. M. Xu, M. M. Harris, C. Ma, Y. S. Liu, X. Wei, H. S. Xu, Y. X. Zhou, Y. C. Cao, K. X. Wang and J. S. Chen, *Adv. Funct. Mater.*, 2016, **26**, 8514.
15 Y. Zhu, S. Wang, Y. Zhong, R. Cai, L. Li and Z. Shao, *J. Power Sources*, 2016, **307**, 552.
16 W. Devina, J. Hwang and J. Kim, *Chem. Eng. J.*, 2018, **345**, 1.
17 L. Yang, X. Li, S. He, G. Du, X. Yu, J. Liu, Q. Gao, R. Hu and M. Zhu, *J. Mater. Chem. A*, 2016, **4**, 10842.
18 F. Lyu, S. Zeng, Z. Sun, N. Qin, L. Cao, Z. Wang, Z. Jia, S. Wu, F. X. Ma, M. Li, W. Wang, Y. Y. Li, J. Lu and Z. Lu, *Small*, 2019, **15**, 1805022.
19 H. Xin, Y. Hai, D. Li, Z. Qiu, Y. Lin, B. Yang, H. Fan and C. Zhu, *Appl. Surf. Sci.*, 2018, **441**, 69.
20 D. Wang, T. Guo and Z. Wu, *ACS Sustainable Chem. Eng.*, 2018, **6**, 13995.
21 X. Zeng, X. Gao, G. Li, M. Sun, Z. Lin, M. Ling, J. Zheng and C. Liang, *J. Mater. Chem. A*, 2018, **6**, 17142.
22 C. Wu and J. Li, *ACS Appl. Mater. Interfaces*, 2017, **9**, 41314.
23 D. Hou, S. Zhu, H. Tian, H. Wei, X. Feng and Y. Mai, *ACS Appl. Mater. Interfaces*, 2018, **10**, 40800.
24 B. Yu, D. Yang, Y. Hu, J. He, Y. Chen and W. He, *Small Methods*, 2019, **3**, 1800287.
25 M. Zhang, X. Huang, H. Xin, D. Li, Y. Zhao, L. Shi, Y. Lin, J. Yu, Z. Yu, C. Zhu and J. Xu, *Appl. Surf. Sci.*, 2019, **473**, 352.
26 T. Thomberg, A. Jänes and E. Lust, *Electrochim. Acta*, 2010, **55**, 3138.
27 L. Yang, X. Li, Y. Ouyang, Q. Gao, L. Ouyang, R. Hu, J. Liu and M. Zhu, *ACS Appl. Mater. Interfaces*, 2016, **8**, 19987.
28 X. Yang, Q. Li, H. Wang, J. Feng, M. Zhang, R. Yuan and Y. Chai, *Chem. Eng. J.*, 2018, **337**, 74.

© 2021 The Author(s). Published by the Royal Society of Chemistry

29 X. Liu, Z. Li, S. Zhang, H. Long, H. Wei, H. Zhang, H. Li and C. Zhao, *Ceram. Int.*, 2017, **43**, 14446.

30 V. Augustyn, J. Come, M. A. Lowe, J. W. Kim, P. L. Taberna, S. H. Tolbert, H. D. Abruña, P. Simon and B. Dunn, *Nat. Mater.*, 2013, **12**, 518.

31 J. Ni, S. Fu, C. Wu, Y. Zhao, J. Maier, Y. Yu and L. Li, *Adv. Energy Mater.*, 2016, **6**, 1502568.

32 X. Li, G. Wu, X. Liu, W. Li and M. Li, *Nano Energy*, 2017, **31**, 1.

33 Y. Zhang, Y. Meng, K. Zhu, H. Qiu, Y. Ju, Y. Gao, F. Du, B. Zou, G. Chen and Y. Wei, *ACS Appl. Mater. Interfaces*, 2016, **8**, 7957.

34 M. Cao, L. Gao, X. Lv and Y. Shen, *J. Power Sources*, 2017, **350**, 87.

35 Y. Zhu, X. Xu, G. Chen, Y. Zhong, R. Cai, L. Li and Z. Shao, *Electrochim. Acta*, 2016, **211**, 972.

36 M. Yousaf, Y. Wang, Y. Chen, Z. Wang, A. Firdous, Z. Ali, N. Mahmood, R. Zou, S. Guo and R. P. S. Han, *Adv. Energy Mater.*, 2019, **9**, 1900567.

37 B. Luo, Y. Hu, X. Zhu, T. Qiu, L. Zhi, M. Xiao, H. Zhang, M. Zou, A. Cao and L. Wang, *J. Mater. Chem. A*, 2018, **6**, 1462.

38 Y. Xu, K. Chu, Z. Li, S. Xu, G. Yao, P. Niu and F. Zheng, *Dalton Trans.*, 2020, **49**, 11597.